

Smectic and nematic phase modulations and transitions under electron beam in $\text{Tb}_2\text{Cu}_{0.83}\text{Pd}_{0.17}\text{O}_4$ Wei Wang,^{1,2,3} Kai Sun,⁴ Yuzki M. Oey,⁵ Robert J. Cava,⁵ Lijun Wu,³ Yimei Zhu,³ Richeng Yu,^{1,2,*} and Jing Tao^{3,†}¹Beijing National Laboratory of Condensed Matter Physics, Institute of Physics, Chinese Academy of Sciences, Beijing 100190, China²School of Physics Sciences, University of Chinese Academy of Sciences, China³Condensed Matter Physics and Materials Sciences Division, Brookhaven National Laboratory, Upton, New York 11973, USA⁴Department of Physics, University of Michigan, Ann Arbor, Michigan 48109, USA⁵Department of Chemistry, Princeton University, Princeton, New Jersey 08540, USA

(Received 23 October 2018; published 12 September 2019)

Understanding the structural origin of the functionality in cuprates has attracted tremendous attention over several decades. In particular, probing distortions in the Cu-O bonding is of great importance for exploring the coupling between the charge and the lattice, a key mechanism for superconductivity and other functionality in correlated materials. Here we study a superlattice modulation in the $\text{Tb}_2\text{Cu}_{0.83}\text{Pd}_{0.17}\text{O}_4$ “214” material, which possesses no superconductivity itself but has the parent structure of the $R_2\text{CuO}_4$ (R = a rare-earth element) superconducting cuprate group. Using transmission electron microscopy (TEM), we find that this superlattice modulation is formed by Cu ion displacements in a direction perpendicular to the Cu-O planes. The superlattice modulation undergoes a reversible electronic smectic-nematic phase transition under electron-beam illumination. With the help of *in situ* TEM results, our findings imply that the superlattice modulation in this material arises from spatially modulated charge ordering at the Cu sites.

DOI: [10.1103/PhysRevMaterials.3.093601](https://doi.org/10.1103/PhysRevMaterials.3.093601)

I. INTRODUCTION

Rare-earth cuprates, $R_2\text{CuO}_4$, where R denotes a rare-earth element, are known to exist for R 's ranging from La to Eu. These materials exhibit extremely interesting physical properties, such as high-temperature superconductivity with hole doping or electron doping [1–4]. La_2CuO_4 , for instance, has been extensively studied as a p -type high-temperature superconductor when doped with excess oxygen or a divalent cation [5–7]. The compounds with $R = \text{Pr}, \text{Nd}, \text{Sm}$, and Eu are n -type high-temperature superconductors when the R cations are partially substituted by tetravalent cations [8–10]. However, $R_2\text{CuO}_4$ with $R = \text{Gd}$ and heavier, e.g., Gd_2CuO_4 and Tb_2CuO_4 , do not become superconducting through any known doping [11]. Despite the absence of superconductivity, Tb_2CuO_4 still attracts considerable interest due to its unique structure and properties [12–14].

From the structural point of view, Tb_2CuO_4 is a representative of one of the three structure types found for $R_2\text{CuO}_4$ compounds, distinguished by differences in configuration between the two-dimensional CuO_2 planes and the apical oxygen atoms adjacent to the CuO_2 planes, along the c axis [15]. The three structural phases are the following: (1) the T phase with CuO_6 octahedra, e.g., in La_2CuO_4 with the $Cmca$ space group [16,17], where CuO_6 octahedra are found, with one oxygen above and one below each of the CuO_4 “plaquettes” in the CuO_2 planes; (2) the T* phase with CuO_5 pyramids, e.g., in $(\text{Nd}_{0.66}\text{Ce}_{0.205}\text{Sr}_{0.135})_2\text{CuO}_4$ with the $P4/nmm$ space group [18], where each CuO_4 plaquette has

one apical oxygen atom, either one at the top or one at the bottom; and (3) the T' phase with CuO_2 square planes only (in Tb_2CuO_4 and Gd_2CuO_4 with $I4/mmm$ space group) without apical oxygen atoms [19]. These configurations of the CuO_4 plaquettes and apical oxygen atoms play an essential role in the structural stability and electronic properties of the materials. For example, the Cu-O stretched bonds may imply a tendency towards electron doping and lead to different Cu electronic structure arrangements in $R_2\text{CuO}_4$ compounds [20–22]. Hence, structural characterizations of Tb_2CuO_4 as a representative of T' cuprates, is important to the understanding of the rare-earth-cuprate $R_2\text{CuO}_4$ group.

However, Tb_2CuO_4 is normally synthesized under high pressure and probing its structural phases under ambient pressure is challenging due to the possible structure relaxation [11,23]. Recently, however, it was reported that a T' type Tb_2CuO_4 material with partial substitution of Pd for Cu can be obtained at ambient pressure; the refined formula of the material is $\text{Tb}_2\text{Cu}_{0.83}\text{Pd}_{0.17}\text{O}_4$ [24]. The previous work employed synchrotron x-ray, TEM, and other property measurements to demonstrate that $\text{Tb}_2\text{Cu}_{0.83}\text{Pd}_{0.17}\text{O}_4$ is an n -type semiconductor and that its structure belongs to the $Pbca$ space group. Specifically, a structural modulation that is long-range in real-space with unidirectional wave vector was observed at a wide range of temperatures. This stripelike superlattice structure in $R_2\text{CuO}_4$ compounds has been widely reported for a variety of R elements [11,25,26]. It was proposed that this stripelike superstructure may be related to the superconductivity through the symmetry breaking of the electronic structures and the crystal lattice [27–29]. Nevertheless, the origin of the superlattice remain elusive, mainly because its characterization is lacking. In particular, oxygen deficiency and migration, or atomic displacements of the R elements,

*rcyu@iphy.ac.cn

†jtao@bnl.gov

were suggested as causes for the superstructure without clear evidence. Therefore improved characterization of the superstructure is urgently needed for a better understanding of this ubiquitously existing phase in $R_2\text{CuO}_4$ compounds.

In the present paper, we show that the superstructure arises from the Cu displacements in $\text{Tb}_2\text{Cu}_{0.83}\text{Pd}_{0.17}\text{O}_4$. We further demonstrate that the superstructure undergoes electronic liquid-crystal (ELC) phase transitions under electron illumination. Using *in situ* heating and cooling TEM observations, we rule out oxygen deficiency as the origin of the phase transitions of the superstructure, but infer that the transition mechanism is related to the modification of carrier concentration in the compound.

In this study, we use the classifications of ELC phases for the following benefits. Firstly, the observed symmetry breaking of the stripe phase upon electron beam illumination matches very well with the description of the ELC phase transitions from smectic (stripe) to nematic to isotropic phases [30]. Secondly, advanced knowledge can be obtained from the developed theory for the ELC phases, such as the role of charge in the commensurate-incommensurate phase transition, providing insight into the origin of the superlattice. In addition, ELC phases are more and more frequently used to describe the electronic structures in cuprate superconductors in recent studies [28,31–33]. The findings here may shed light on the relationship between the symmetry breaking of the crystal lattice and the electronic structures in the cuprates.

II. RESULTS AND DISCUSSION

The synthesis method for $\text{Tb}_2\text{Cu}_{0.83}\text{Pd}_{0.17}\text{O}_4$ and its crystal structure can be found in Ref. [24]. Selected-area electron diffraction patterns were used to identify the crystal symmetry and the unidirectional superstructure. The right panels of Figs. 1(a) and 1(b) show experimental electron diffraction patterns along the [001] and [011] zone axes, respectively. The diffraction patterns were obtained from *the same area* in one thin sample flake by tilting about 25° along the a_o axis (a_o denotes the fundamental lattice parameter in the orthorhombic crystal structure). According to the symmetry operations of the $Pbca$ space group, the reflections [marked by yellow circles in Fig. 1(a)], such as (010), (100), which should be extinct, are clearly seen in Fig. 1(a), due to the multiple scattering of the electron beam along the low-index zone. More interestingly, sharp superlattice reflections (marked by red circles) with an incommensurate modulation ($\sim 0.473 a^*$) in the a_o direction are shown in Fig. 1(b). These are an intrinsic characteristic of this material's structure. From the ELC classification, the superstructure breaks the translational symmetry along the a_o direction with respect to the fundamental lattice, which can be classified as a stripe (electronic smectic) phase.

Combining the diffraction patterns taken from one sample flake, we propose a crystal structure model for the stripe phase in this material using a superstructure refinement by adjusting the length of the Cu-O bond. (The initial structure model reported for this material [24] does not provide the structure of the superlattice modulation.) Note that Cu and Pd atoms are randomly distributed on the Cu sites and are indistinguishable by our techniques. If a longitudinal displacement is added in the direction of the modulation wave vector, i.e., in the

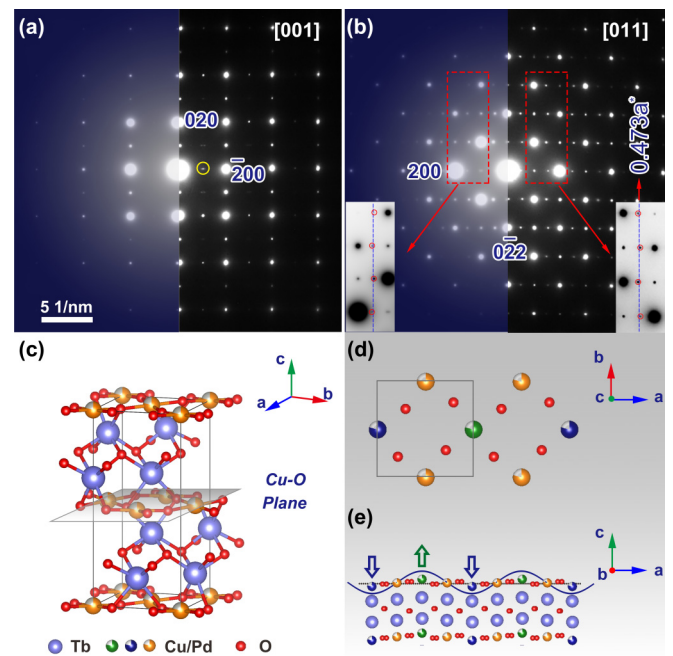


FIG. 1. Two typical electron diffraction patterns obtained from (a) [001] and (b) [011] zone axes of the same sample flake of $\text{Tb}_2\text{Cu}_{0.83}\text{Pd}_{0.17}\text{O}_4$ (left: electron diffraction dynamic simulations of the refined crystal structure; right: experimental patterns). Note that dynamic electron diffraction simulations employ Bloch wave methods with incommensurate wave vector for superstructural modulation of the structure, assuming a sinusoidal displacement wave. The peak marked by the yellow circle in (a) is due to crystalline domains. The additional satellite peaks in (b) marked by the red circles indicate an incommensurate modulation q_1 along the a^* wave vector in $\text{Tb}_2\text{Cu}_{0.83}\text{Pd}_{0.17}\text{O}_4$. The blue dashed lines indicate the position of wave number $q = 0.5$. (c) A parent crystal structure of $\text{Tb}_2\text{Cu}_{0.83}\text{Pd}_{0.17}\text{O}_4$ based on the $Pbca$ space group. (d) Extracted Cu-O plane from (c), the structure in the grey frame presents a unit cell in (c). (e) Schematic crystal structure in the a - c plane. One of the Cu atoms (green sphere) in the Cu-O plane moves along the out-of-plane c_o direction; two other Cu atoms (dark blue spheres) in the same row shift in the opposite direction while the rest of the atoms (orange spheres) in one Cu-O layer remain the same as in (c). Note that the new symmetry of the superstructure is lowered compared to the original $Pbca$ space group.

a_o direction, then (100) modulation reflections should be observed along both of the [001] and [011] zone axes. However, in our experimental diffraction patterns, the incommensurate modulation in the a_o direction with a modulation wave vector $\mathbf{q}_1 = (0.473, 0, 0)$ is only shown along the [011] zone axis; it is not observed along the [001] direction. This clearly indicates that any atomic displacements in the Cu-O planes with a noticeable amplitude can be excluded. Thus the only possible model of the displacement is out of the Cu-O plane, shown in the crystal models in Fig. 1(c). Note that the intensities of the superlattice reflections are fairly strong, indicating that Cu out-of-plane displacements are much more likely their origin than O out-of-plane displacements in this case. To further explore the proposed crystal structure model, we obtained a HAADF-STEM image, which is sensitive to atomic number Z and atomic displacements, along the [010] zone axis, a

crystallographic orientation that is perpendicular to the wave propagation direction and the proposed Cu displacement. As shown in Fig. S1 in Ref. [34], the Cu displacements along the c_o axis are clearly seen. Hence the origin of the superlattice is an out-of-plane Cu-O distortion.

The out-of-plane lattice distortion of Cu-O bonding in $\text{Tb}_2\text{Cu}_{0.83}\text{Pd}_{0.17}\text{O}_4$ manifests a novel model that has attracted little previous attention. To our knowledge, most of the Cu-O distortions observed have been in-plane. Thus the Cu-O plane is identified as a two dimensional correlated metallic state via hole or electron doping and the superconducting plane at low temperatures [35,36]. Tremendous efforts, both in experiments and theory, have been put into probing the spin-spin interaction, electron-electron correlation, and/or electron-phonon coupling in superconducting cuprates, and all of those interactions are in the Cu-O plane only [21,28,36–38]. Our results, with the distinctive Cu-O distortion out-of-plane, add more possibilities into the experimental analysis and theoretical considerations, and may advance the understanding of superconductivity in cuprates. In addition, the characterization of the Cu-O distortion may help to explain the role of Pd substitution in stabilizing the T'-type structure at ambient pressure. Nearly 20% Pd is substituted for Cu in the Cu-O plane, which consequently introduces an extra strain due to the size mismatch between Cu and Pd. In particular, the ionic radii of Cu^{2+} and Pd^{2+} are 87 and 100 pm, respectively (i.e., Shannon and Prewitt, 1969) [39]. It is reasonable to infer the out-of-plane displacement of Cu and CuO_4 square rotation in the Cu-O plane and even electron density redistribution as a result of the in-plane strain induced by the extra Pd, especially given the fact that the absence of apical oxygens will provide more space for the movement of Cu in the T' structure than the T and T* structures. Moreover, other T' type cuprates prepared at high pressure were observed to have similar superstructures [11], indicating that out-of-plane Cu-O distortions could be generic in this type of cuprate. Moreover, it is believed by many researchers that one of the primary contributors for superconductivity in these materials is a consequence of the strong hybridization of Cu $d_{x^2-y^2}$ and O $p_{x,y}$ orbitals. The other orbitals like Cu $d_{z^2-r^2}$ make less contributions [1,40]. In our case, the out-of-plane displacement would weaken the Cu-O in-plane hybridization strength and may preclude the realization of superconductivity.

To further explore the origin of the superstructure, we take high-resolution TEM images, observing a distinct stripe phase along the [011] zone axis at room temperature (RT). During the electron beam illumination, observing a phase transition from stripe phase (smectic) to nematic phase for superstructures as a function of both the electron dose rate and operating time is unexpected. However, that is the case here. The observations are summarized in Fig. 2. Using the electron beam of 200 kV with dose rate of $1.1 \times 10^6 \text{ e}^- \text{ s}^{-1} \text{ nm}^{-2}$ on the specimen, the stripe phase [the unidirectional superstructure is highlighted by the solid white lines in Fig. 2(a)] was observed to gradually transform into a nematic phase at the edge (relatively thinner areas) of the sample flake first, then at the inner areas (relatively thicker) in a time duration about 130s [Figs. 2(a)–2(c)]. The nematic phase here is indicated by the appearance of short-range superstructures in the orthogonal direction with respect to the original long-

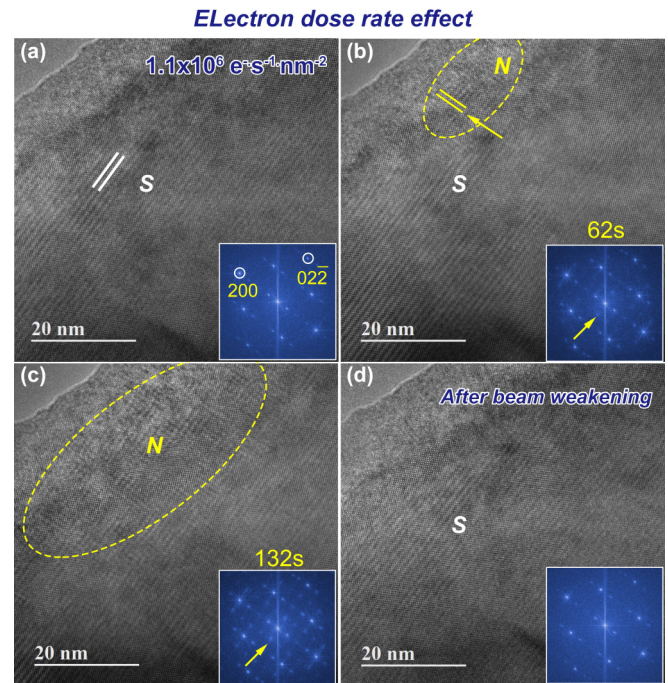


FIG. 2. Stripe (smectic)-nematic phase transition process for $\text{Tb}_2\text{Cu}_{0.83}\text{Pd}_{0.17}\text{O}_4$ (in the same area) under an electron dose rate of $1.1 \times 10^6 \text{ e}^- \text{ s}^{-1} \text{ nm}^{-2}$ with a 200 kV accelerating voltage at RT. (a) Initial stripe phase (S) along the a_o axis before phase transition, the solid white lines indicate the unidirectional superlattice. (b) and (c) HRTEM images as a function of time, the yellow arrow indicates the orthogonal short-range superlattice induced by the electron beam illumination, the areas circled with dashed yellow lines indicate the formation of the nematic phase (N). (d) The recovered stripe phase after lowering the dose rate. The inserts are FFT diffractograms of each entire image. The intensities of the newly formed peaks marked by yellow arrows reflect the transition process. The numbers in (b) and (c) are the illumination time under the high dose rate.

range stripe phase. Meanwhile, the fast Fourier transform (FFT) diffractogram of the entire image shows that the peaks associated with the stripe phase gradually become diffuse and additional diffuse peaks (yellow arrows) associated with the orthogonal superstructures emerge as a function of time, which is consistent with the electronic smectic-nematic phase transition. We want to emphasize that, although ELC phases normally refer to the global state of the material, the ELC phases we describe here are at the mesoscale, i.e., the nematic phase may also be described as a phase separation of two types of short-range phases with their superstructures orthogonal to each other. In other words, during the observations, the entire sample may still remain in the electronic smectic phase, while the sample at the edge/thin areas are “globally” nematic. As the illumination time increases, the nematic phase expands into the thicker area and becomes more “global” [Figs. 2(b) and 2(c)]. A series of electron diffraction patterns during the beam-induced smectic-nematic phase transition is shown in Fig. S2 [34].

It is worth noting that the electron-beam-induced smectic-nematic phase transition is reversible and repeatable. After 210 seconds of beam illumination, we lowered the dose rate

Temperature effect

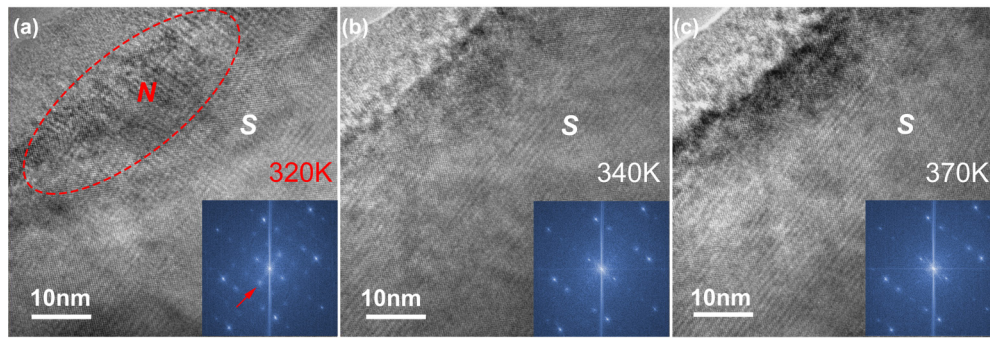


FIG. 3. Final states after electron beam illumination in heating experiments. A $\text{Tb}_2\text{Cu}_{0.83}\text{Pd}_{0.17}\text{O}_4$ sample flake is irradiated with the same dose rate ($1.1 \times 10^6 \text{ e}^- \text{ s}^{-1} \text{ nm}^{-2}$), in the same area, at the same magnification, but at different temperatures. (a) Smectic-nematic phase transition is reproduced under irradiation at 320 K, the area circled by the red dotted line is the nematic phase induced by the electron beam illumination, the peak highlighted by a red arrow in the FFT diffractogram of the entire image also indicates the appearance of the nematic phase. (b) and (c) The nematic phase is precluded to emerge in $\text{Tb}_2\text{Cu}_{0.83}\text{Pd}_{0.17}\text{O}_4$ at higher temperatures (340 and 370 K).

to $4.1 \times 10^4 \text{ e}^- \text{ s}^{-1} \text{ nm}^{-2}$; with such an electron dose rate, no clear contrast of superstructures was shown on TEM images. The change can still be seen in the FFT diffractogram) on waiting for 200 s. As a result, the already formed nematic phase gradually disappears and the sample goes back to the original stripe phase. We quickly increased the electron dose rate so that clear TEM images can be taken, as shown in Fig. 2(d). The same smectic-nematic phase transition and the recovery of the smectic phase were observed by repeating the operation at higher electron dose rates for a long time, by the “beam-blank” operation, for many cycles (see Fig. S3 for more observations from sequence cycles and video S1 for real-time recording [34]). The above observations are representative for this material based on the TEM recordings from many sample flakes, i.e., we rule out the compositional inhomogeneity as the cause of the superstructure and the beam-induced effects.

Electron-beam-induced effects are sometimes attributed to the beam heating processes due to the inelastic scattering [41,42]. However, we find that beam-heating cannot be the dominant mechanism for the observations in Fig. 2 by performing *in situ* heating TEM experiments. The results are demonstrated in Fig. 3. We recorded HRTEM images through the beam-dose-rate controlled cycles at various temperatures when the sample reached a thermal stability. We first note that, under a low electron dose rate, the stripe phase remains long-range upon warming, i.e., no smectic-nematic phase transition was observed under solely thermal fluctuations. Upon warming, a similar smectic-nematic phase transition can be induced by high electron dose rate at the sample temperature, ranging from room-temperature to about 320 K [Fig. 3(a)]. When the sample temperature is about 340 K [Fig. 3(b)] and above [Fig. 3(c)]; more results can be found in Fig. S4 and video S2 [34]), where it can be seen that the stripe phase (smectic) becomes stable no matter how high the electron dose rate is and how long the sample is under illumination. In addition, *in situ* low-temperature experiments were performed using a liquid-nitrogen cooling stage and the observations of beam-induced smectic-nematic phase transition were reproduced as well at the sample temperature of 90 K (detailed analysis is

shown in Fig. S5 [34]). Based on the *in situ* observations the electron-beam-induced smectic-nematic phase transition only occurs in a certain temperature range, and therefore cannot be due to a heating mechanism.

Since the influence of beam heating is eliminated, we examined other possible electron-beam-induced effects, particularly electron-irradiation damage, including knock-on damage (structure damage and mass loss), electron radiolysis and contamination, by correlating them with the experimental observations [41–43]. Firstly, we can rule out contamination and the mass loss, as both are nonreversible effects, since the observed transition upon beam illumination is reversible and repeatable. Secondly, knock-on damage is an effect that becomes weakened with lowered incident electron accelerating voltage. To test the mechanism, we performed the TEM experiments using 80 kV accelerating voltage at RT and the reversible smectic-nematic transition was reproduced, however, under only half of the dose rate ($0.5 \times 10^6 \text{ e}^- \text{ s}^{-1} \text{ nm}^{-2}$) compared with that under 200 kV (see Fig. S6 in Ref. [34]). That is, the electron-irradiation effect is strengthened with lowered accelerating voltage in this case, which is evidence against the knock-on damage mechanism. Finally, since the electron radiolysis effect, an effect of beam ionization on the electrons to be liberated from the material’s constituent atoms, is known to become more pronounced under lower accelerating voltage, we propose electron radiolysis to be the mechanism of the beam-induced smectic-nematic transition in the sample. Commonly in TEM operations, a certain number of secondary electrons and Auger electrons would be generated and escape from the sample, depending on the electric conductivity of the material [41–44]. Since the sample is under continuous electron illumination, a dynamic charge balance can be established in a short time based on the electron dose rate, the electrical conductivity of the sample and the environment [43]. As a result, the carrier concentration in the sample would vary and charge would redistribute in the crystal, which could affect the Cu-O bonding and result in a lattice distortion.

Nevertheless, it is interesting to understand the temperature-dependent behavior of the transition, i.e., how it is that the beam-induced smectic-nematic transition

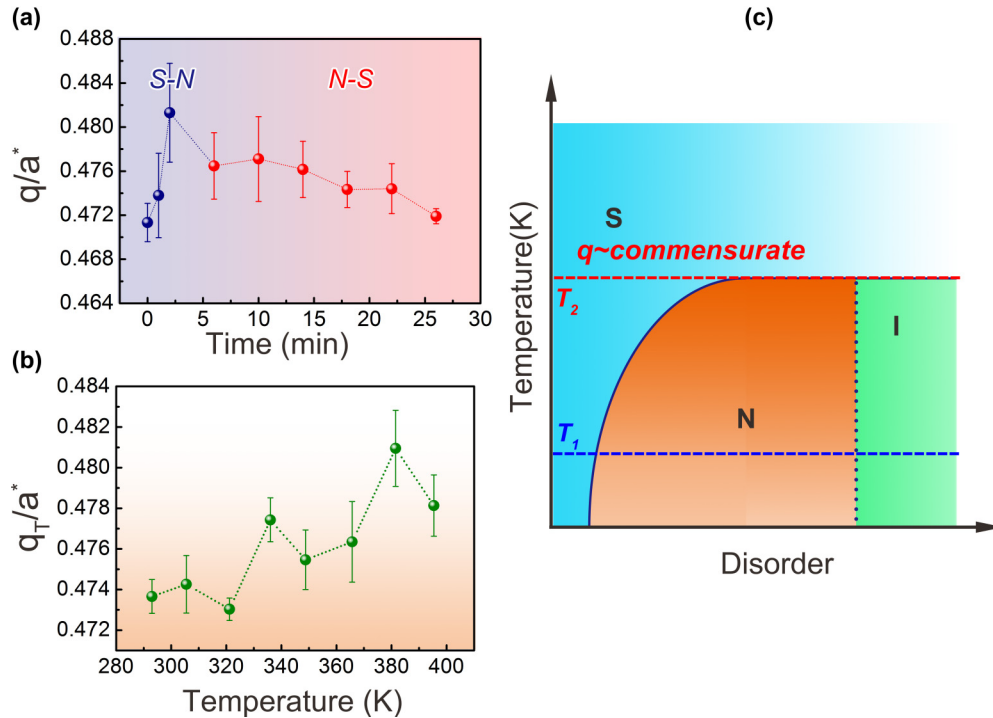


FIG. 4. (a) The wave vectors \mathbf{q} of the modulations along \mathbf{a}^* as a function of illumination time during the S-N-S phase transitions, measured using electron diffraction patterns at the [011] zone axis. (b) The wave vector q_T (T : temperature) along \mathbf{a}^* measured at different temperatures. (c) Schematic phase diagram as a function of disorder generated by electron illumination. S, N, and I are for smectic, nematic, and isotropic phases, respectively. The dotted line between the nematic and isotropic phases indicates the uncertainty of the line position, a detail that is beyond the scope of the current study. Based on our experimental observations, the temperature T_1 is lower than 340 K, and the value of q is close to a commensurate number at the temperature of T_2 .

(observed at RT) cannot take place at the temperature higher than a certain value. We note that the theory for ELC phases has proposed that introducing charge disorder can cause the smectic-nematic transition [45]. The ELC theory also suggests that when the wave vector of an ordered structure become commensurate, the smectic phase would be more resistant to the charge perturbations when compared to the cases with incommensurate wave vectors. In view of the developed ELC theory, we measure the wave number q of the unidirectional superstructure under various conditions (temperatures, electron dose rates and phases). To accurately measure the wave number, snapshots of electron diffraction patterns, instead of using FFT of the HRTEM images, were captured during the smectic-nematic phase transition under high electron dose rate and the relaxation of the nematic phase back to smectic under low electron dose rate. Within the error bars of the measurements, the q values increase during the smectic-nematic phase transition and gradually go back to the initial value after the recovery, as plotted in Fig. 4(a). In addition, the measurement of wave number q_T as a function of temperature [Fig. 4(b)] shows that the q value monotonically increases to become closer to a commensurate value (0.5) upon warming. Hence our observations are consistent with the prediction of the phenomenological ELC theory [45] that a commensurate modulation could be more resistant to charge variation than an incommensurate one. Moreover, we construct a phase diagram in Fig. 4(c) to outline the experimental observations using the classification of ELC phases. Note that, when the superlattice reflections have

nearly equal intensities in the orthogonal directions, the phase can be identified as an electronic isotropic phase.

All the evidence above has an important implication about the nature of the superstructure in $\text{Tb}_2\text{Cu}_{0.83}\text{Pd}_{0.17}\text{O}_4$, namely, that it appears to arise from a modification in the charge density states of the Cu/Pd ions. Experimental observations indicate that neither compositional order nor oxygen vacancies are the origin of the superstructure. In addition, we identify the role of electron illumination in this study and explain the temperature-dependent observations. Since the superstructure undergoes a reversible phase transition by means of manipulation of the charge degree of freedom, this leads to the conclusion that charge order on the Cu/Pd ion sites is the origin, for ions that are well known to display valence states, in the superstructure in this material.

III. CONCLUSIONS

To summarize, we study a unidirectional superlattice modulation in $\text{Tb}_2\text{Cu}_{0.83}\text{Pd}_{0.17}\text{O}_4$ by using *in situ* TEM techniques. The results strongly indicate that the distortion leading to the modulation, common in the family of R_2CuO_4 cuprates, is the Cu-O bonding that is out of the Cu-O plane. This is lattice distortion is novel compared with the conventional in-plane Cu-O distortion seen in other cuprates. In addition, an electron-beam-induced electronic smectic-nematic phase transition was observed and analyzed in this material. Among the possible electron illumination effects, radiolysis is identified to be the driving force for the smectic-nematic transition.

Such observations further imply that charge ordering on the Cu sites may be the fundamental origin of the superstructure in this material.

ACKNOWLEDGMENTS

R.Y. and W.W. would like to acknowledge the financial support by the National Key Research Program of China (Grants No. 2017YFA0206200 and No. 2016YFA0300701), the National Natural Science Foundation of China (Grants No. 11874413 and No. 11574376) and China Scholarship Council for support of W.W. to study abroad. The electronic

microscopy work was carried out at Brookhaven National Laboratory (BNL) and sponsored by the US Department of Energy (DOE) basic Energy Sciences (BES), by the Materials Sciences and Engineering Division under Contract DE-SC0012704. It was also supported by the resources of Center for Functional Nanomaterials at BNL. K.S. was supported in part by NSF under Grant No. ECCS-1307744 and the MCubed program at University of Michigan. The work at Princeton University was supported by National Science Foundation (Platform for the Accelerated Realization, Analysis, and Discovery of Interface Materials (PARADIM) under Cooperative Agreement No. DMR-1539918).

-
- [1] P. W. Anderson, *Science* **235**, 1196 (1987).
- [2] M. B. Maple, *Mrs. Bull.* **15**, 60 (1990).
- [3] D. Reznik, L. Pintschovius, M. Ito, S. Iikubo, M. Sato, H. Goka, M. Fujita, K. Yamada, G. Gu, and J. Tranquada, *Nature (London)* **440**, 1170 (2006).
- [4] M. Brinkmann, T. Rex, H. Bach, and K. Westerholt, *Phys. Rev. Lett.* **74**, 4927 (1995).
- [5] B. Wells, Y. Lee, M. Kastner, R. Christianson, R. Birgeneau, K. Yamada, Y. Endoh, and G. Shirane, *Science* **277**, 1067 (1997).
- [6] X. Zhou, P. Bogdanov, S. Kellar, T. Noda, H. Eisaki, S. Uchida, Z. Hussain, and Z.-X. Shen, *Science* **286**, 268 (1999).
- [7] Y. S. Lee, R. J. Birgeneau, M. A. Kastner, Y. Endoh, S. Wakimoto, K. Yamada, R. W. Erwin, S.-H. Lee, and G. Shirane, *Phys. Rev. B* **60**, 3643 (1999).
- [8] Y. Krockenberger, J. Kurian, A. Winkler, A. Tsukada, M. Naito, and L. Alff, *Phys. Rev. B* **77**, 060505(R) (2008).
- [9] J. Gauthier, S. Gagné, J. Renaud, M.-E. Gosselin, P. Fournier, and P. Richard, *Phys. Rev. B* **75**, 024424 (2007).
- [10] O. Matsumoto, A. Utsuki, A. Tsukada, H. Yamamoto, T. Manabe, and M. Naito, *Phys. Rev. B* **79**, 100508(R) (2009).
- [11] P. Bordet, J. Capponi, C. Chailout, D. Chateigner, J. Chenavas, T. Fournier, J. Hodeau, M. Marezio, M. Perroux, and G. Thomas, *Physica C* **193**, 178 (1992).
- [12] M. Tovar, X. Obradors, F. Pérez, S. Oseroff, R. Duro, J. Rivas, D. Chateigner, P. Bordet, and J. Chenavas, *J. Appl. Phys.* **70**, 6095 (1991).
- [13] M. Tovar, X. Obradors, F. Pérez, S. B. Oseroff, R. J. Duro, J. Rivas, D. Chateigner, P. Bordet, and J. Chenavas, *Phys. Rev. B* **45**, 4729 (1992).
- [14] J. Mira, J. Castro, J. Mahia, C. Vázquez-Vázquez, M. López-Quintela, J. Rivas, and S. Oseroff, *J. Non-cryst. Solids.* **172–174**, 491 (1994).
- [15] Y. Tokura, H. Takagi, and S. Uchida, *Nature (London)* **337**, 345 (1989).
- [16] Y. Xue, P. Hor, R. Meng, Y. Tao, Y. Sun, Z. Huang, L. Gao, and C. Chu, *Physica C: Superconductivity* **165**, 357 (1990).
- [17] M. Reehuis, C. Ulrich, K. Prokeš, A. Gozar, G. Blumberg, S. Komiyama, Y. Ando, P. Pattison, and B. Keimer, *Phys. Rev. B* **73**, 144513 (2006).
- [18] H. Sawa, S. Suzuki, M. Watanabe, J. Akimitsu, H. Matsubara, H. Watabe, S.-i. Uchida, K. Kokusho, H. Asano, and F. Izumi, *Nature (London)* **337**, 347 (1989).
- [19] H. M. Luo, Y.-Y. Hsu, B. N. Lin, Y. P. Chi, T. J. Lee, and H. C. Ku, *Phys. Rev. B* **60**, 13119 (1999).
- [20] F. Carbone, D.-S. Yang, E. Giannini, and A. H. Zewail, *Proc. Natl. Acad. Sci. USA* **105**, 20161 (2008).
- [21] J. Lee, K. Fujita, K. McElroy, J. Slezak, M. Wang, Y. Aiura, H. Bando, M. Ishikado, T. Masui, and J.-X. Zhu, *Nature (London)* **442**, 546 (2006).
- [22] J. Song and J. F. Annett, *Phys. Rev. B* **51**, 3840 (1995).
- [23] P. Bordet, J. Capponi, C. Chailout, D. Chateigner, J. Chenavas, T. Fournier, J. Hodeau, M. Marezio, K.M. Perroux, and G. Thomas, *Physica C: Superconductivity* **185–189**, 539 (1991).
- [24] Y. M. Oey, J. E. Park, J. Tao, E. M. Carnicom, T. Kong, M. B. Sanders, and R. Cava, *J. Mater. Res.* **33**, 1690 (2018).
- [25] F. Izumi, Y. Matsui, H. Takagi, S. Uchida, Y. Tokura, and H. Asano, *Physica C* **158**, 433 (1989).
- [26] C. Chen, D. Werder, A. James, D. Murphy, S. Zahurak, R. Fleming, B. Batlogg, and L. Schneemeyer, *Physica C* **160**, 375 (1989).
- [27] S. Rajasekaran, J.-i. Okamoto, L. Mathey, M. Fechner, V. Thampy, G. D. Gu, and A. Cavalleri, *Science* **359**, 575 (2018).
- [28] J. Tranquada, B. Sternlieb, J. Axe, Y. Nakamura, and S. Uchida, *Nature (London)* **375**, 561 (1995).
- [29] J. M. Tranquada, K. Nakajima, M. Braden, L. Pintschovius, and R. J. McQueeney, *Phys. Rev. Lett.* **88**, 075505 (2002).
- [30] J. Tao, K. Sun, W.-G. Yin, L. Wu, H. Xin, J. Wen, W. Luo, S. Pennycook, J. Tranquada, and Y. Zhu, *Sci. Rep.* **6**, 37624 (2016).
- [31] V. Hinkov, D. Haug, B. Fauqué, P. Bourges, Y. Sidis, A. Ivanov, C. Bernhard, C. Lin, and B. Keimer, *Science* **319**, 597 (2008).
- [32] Y. Ando, K. Segawa, S. Komiyama, and A. N. Lavrov, *Phys. Rev. Lett.* **88**, 137005 (2002).
- [33] A. Mesaros, K. Fujita, H. Eisaki, S. Uchida, J. Davis, S. Sachdev, J. Zaanen, M. Lawler, and E.-A. Kim, *Science* **333**, 426 (2011).
- [34] See Supplemental Material at <http://link.aps.org/supplemental/10.1103/PhysRevMaterials.3.093601> for experimental data analysis of a HAADF-STEM image, electron diffraction patterns during phase transitions, *in situ* TEM observations and descriptions of experimental video.
- [35] R. J. McQueeney, J. L. Sarrao, P. G. Pagliuso, P. W. Stephens, and R. Osborn, *Phys. Rev. Lett.* **87**, 077001 (2001).
- [36] P. Zhang, S. G. Louie, and M. L. Cohen, *Phys. Rev. Lett.* **98**, 067005 (2007).
- [37] S. Ishihara and N. Nagaosa, *Phys. Rev. B* **69**, 144520 (2004).
- [38] Y. Kubo, F. R. Ong, P. Bertet, D. Vion, V. Jacques, D. Zheng, A. Dréau, J.-F. Roch, A. Auffeves, F. Jelezko, J. Wrachtrup,

- M. F. Barthe, P. Bergonzo, and D. Esteve, *Phys. Rev. Lett.* **105**, 140502 (2010).
- [39] R. T. Shannon and C. T. Prewitt, *Acta Crystallographica Sec. B* **25**, 925 (1969).
- [40] E. Pellegrin, N. Nücker, J. Fink, S. L. Molodtsov, A. Gutiérrez, E. Navas, O. Strebel, Z. Hu, M. Domke, G. Kaindl, S. Uchida, Y. Nakamura, J. Markl, M. Klauda, G. Saemann-Ischenko, A. Krol, J. L. Peng, Z. Y. Li, and R. L. Greene, *Phys. Rev. B* **47**, 3354 (1993).
- [41] R. Egerton, *Ultramicroscopy* **127**, 100 (2013).
- [42] R. Egerton, P. Li, and M. Malac, *Micron* **35**, 399 (2004).
- [43] J. Tao, J. Chen, J. Li, L. Mathurin, J.-C. Zheng, Y. Li, D. Lu, Y. Cao, L. Wu, and R. J. Cava, *Proc. Natl. Acad. Sci.* **114**, 9832 (2017).
- [44] J. Cazaux, *Ultramicroscopy* **60**, 411 (1995).
- [45] L. Nie, G. Tarjus, and S. A. Kivelson, *Proc. Natl. Acad. Sci. USA* **111**, 7980 (2014).